# Tuning Surface Chemistry in 2D Layered BiOI by Facile LiquidPhase Exfoliation for Enhanced Photoelectrocatalytic Oxygen Evolution

# Tuning Surface Chemistry in 2D Layered BiOI by Facile Liquid-phase Exfoliation for Enhanced Photoelectrocatalytic Oxygen Evolution

*Mengjiao Wang,* Jaime Gallego, Micaela Pozzati, and Teresa Gatti**

M. Pozzati, T. Gatti, M. Wang

Dipartimento Scienza Applicata e Tecnologia (DISAT), Politecnico di Torino, Corso Duca degli Abruzzi 24, 10129, Torino, Italy

E-mail: mengjiao.wang@polito.it; teresa.gatti@polito.it

J. Gallego, T. Gatti

Center for Materials Research (LaMa), Justus Liebig University, 35392 Giessen, Germany

Keywords: BiOI, Photoelectrocatalysis, Liquid-phase exfoliation, Surface chemistry, Oxygen evolution reaction

## Abstract

BiOI is a promising photoelectrocatalyst for oxidation reactions. However, the limited photoelectrocatalytic (PEC) activity necessitates the development of new strategies to modify its surface chemistry and thus enhance functional properties. In this work, we present a simple method to increase photocurrent density in a BiOI-based photoanode by exfoliating microspheres of the oxyhalide produced through a microwave-induced hydrothermal synthesis. Following exfoliation in isopropanol, the resulting layered BiOI-based colloid contains a greater variety of species, including $Bi_2O_2CO_3$, $I_3^-$, $IO_3^-$, $Bi^{5+}$ and hydroxide species, compared to the original BiOI. These additional species do not directly enhance the PEC oxygen evolution reaction (OER) performance. Instead, they are consumed or converted during PEC OER, resulting in more active sites on the photoelectrode and reduced resistance, which ultimately improves the water oxidation performance of the exfoliated BiOI. Over long-term chronoamperometry, the exfoliated BiOI demonstrates a photocurrent twice as high as that of the BiOI microspheres. Analysis of the species after PEC OER reveals that the combination of $IO_3^-$, $Bi^{5+}$ and $I_3^-$ species on the BiOI is beneficial for charge transfer, thus enhancing the intrinsic PEC properties of the BiOI. This study offers new insights into the role of surface chemistry in determining PEC performance, aiding optimization of 2D-materials-based photoelectrocatalysts.

## 1. Introduction

BiOI has garnered significant interest as a promising photoelectrocatalyst and attracted increasing attention in recent years due to its unique properties, low toxicity and potential application in various fields including water splitting, pollutant degradation, and $CO_2$ reduction.[1] As a semiconductor material, BiOI exhibits a suitable bandgap and effective exciton dissociation into free-charges under light irradiation.[2,3] Specifically, through the absorption of photons, BiOI generates electron-hole pairs, which can participate in redox reactions at the surface (or interface, if in heterojunctions) of the catalyst.[3] However, in bulk BiOI, the rapid recombination of photogenerated electron-hole pairs and lack of surface active sites can limit the efficiency of photoelectrocatalytic (PEC) reactions.[4,5] Bulk form also hinders the accessibility of reactant molecules to the active sites and can thus reduce the overall rate of PEC reactions.

Surface chemistry plays a pivotal role in the performance of BiOI as a photoelectrocatalyst.[6–8] To improve the PEC properties, various designs of novel BiOI catalysts focusing on modifying the surface chemistry have been performed to separate the photogenerated charges and delay the charge recombination.[9–11] In general, the facet, surface defects and surface species can be tuned by various methods and have been reported to modify PEC properties.[12] For instance, BiOI crystals offer abundant active sites on their {110} facets for generating more $\bullet O^{2-}$ and •OH than {001} facets, thus enhancing the $Hg^0$ oxidation.[13] Besides, plenty of heterojunctions with BiOI were designed to separate the charge efficiently, thus increasing the amount of $\bullet O^{2-}$ and •OH for PEC reactions.[14–16] Moreover, the increasing oxygen vacancies is reported useful to improve the PEC activity of BiOI photocathode, as these vacancies serve as the active sites for trapping photogenerated electrons for PEC reduction reactions.[17] Wang et al. produced oxygen vacancies on BiOI with catechol and proved these oxygen vacancies are crucial for the cathodic photoelectrochemistry of BiOI.[18] Shi et al. reported an electrodeposition method to fabricate intrinsic BiOI photocathode with oxygen vacancies, which significantly increases the ability of $N_2$ adsorption and activation in the PEC $N_2$ reduction.[19] Furthermore, while BiOI synthesized using the traditional hydrothermal method exhibits few surface species[20–23], BiOI subjected to additional treatment steps demonstrates cooperative effects among various surface species, including $IO_3^-$/ $I^-$[24], $Bi^{5+}$ / $Bi^{(3-x)+}$ / oxygen vacancy[25], $Bi_2O_2CO_3$ / $I^-$[26]. However, among these reports, it is difficult to find BiOI as photoanode for oxygen evolution reaction (OER), and this is because the pure BiOI is not very active for PEC OER.[27,28] The photocurrent of pure BiOI typically ranges from 0.1 μA to 10

μA, depending on the synthesis conditions used.[29,30] While many studies focus on enhancing the PEC OER activity of BiOI electrodes by combining BiOI with other materials, there is less research that explores the reasons behind pure BiOI's performance.[29,31,32] Specifically, the surface chemistry of BiOI during PEC OER is barely studied and methods to improve PEC OER activity of BiOI by modifying the surface environment are not fully developed.

BiOI possesses a layered crystal structure with one layer of [$Bi_2O_2$] covalently bonded between two I layers, and these I-$Bi_2O_2$-I sandwich layers are connected with each other by weak van der Waals interaction (see Figure 1a).[33] Noticing the structure of BiOI, bulk BiOI can be easily exfoliated to 2D materials along [001] direction with one or more I-$Bi_2O_2$-I sandwich layers by mechanical force theoretically, which is supposed to expose more active sites for catalytic reactions and change the surface chemistry of the oxyhalide. Liquid phase exfoliation (LPE) is a frequently used and straightforward method to break bulk 2D materials and produce corresponding 2D nanolayers by ultrasonication or shearing force. LPE of BiOBr was reported previously by us, using 1-Methyl-2-pyrrolidone as liquid medium, and the exfoliated BiOBr shows thin layer morphology with width around 50 nm.[34] However, very few reports on LPE of BiOI have been reported yet. Based on this background, we designed an LPE method to produce 2D layered BiOI, finding that the surface species on exfoliated BiOI differ significantly from those on bulk BiOI. The exfoliated BiOI shows an increase in species with higher oxidation states, particularly $CO_3^{2-}$, $I_3^-$, $IO_3^-$, $Bi^{5+}$, and various hydroxide surface species. We then applied this exfoliated BiOI for PEC OER. Surprisingly, the exfoliated BiOI exhibited higher photocurrent compared to bulk BiOI after surface activation in the PEC environment. Analysis of the surface species suggests that most of the ones generated by LPE are eliminated or converted into other species during the catalytic process. This effect increases active sites and reduces resistance, leading to improved PEC OER performance compared to bulk BiOI. However, a small amount of $IO_3^-$ on bulk BiOI remains during chronoamperometric prolonged tests. Along with $Bi^{5+}$ and $I_3^-$, which maintain higher binding energy and a better interface quality, this results in an improved intrinsic capability towards OER in bulk BiOI compared to the exfoliated BiOI nanosheets in the long run.

## 2. Results and discussion

To circumvent the time and energy demands of the hydrothermal method, bulk BiOI (BOI) samples were synthesized via a microwave reaction, as detailed in the experimental section, with ethylene glycol added to produce a variety of surface species.[35] The exfoliated BiOI sample (BOIexf) from BOI was obtained by a facile LPE method. The crystalline structure of

as-prepared samples was determined by X-ray diffraction (XRD) technique. As shown in Figure 1b, all the diffraction peaks of BOI and BOIexf can be ascribed to tetragonal BiOI (ICSD No. 391354), and no other impurities are found in the patterns. The morphology of BOI and BOIexf was characterized by scanning electron microscopy (SEM), as shown in Figure 1c and d. BOI from solvothermal method presents microspheres shape of ~1 μm diameter, with each microsphere composed of thin nanosheets. BOIexf displays instead irregularly dispersed nanosheets with an average size less than 100 nm. Transmission electron microscopy (TEM) imaging confirms a nanosheet morphology of BOIexf in Figure 1e. A typical high-resolution TEM (HRTEM) image, as presented in Figure 1f and 1g, indicates that the lattice fringe of 0.282 nm corresponds to the (110) plane of BiOI. Meanwhile, the fast Fourier transformation (FFT) pattern corresponding to the region in Figure 1f further illustrates that the exfoliated layers can be indexed to BiOI crystal structure with [001] axis (Figure 1g). HRTEM images in Figure 1i and 1j indicate that the exfoliated BiOI are mostly few layers. Interestingly, by calculating the layer distance of BOIexf, it is clear that the (001) layer distance (0.947 nm) is enlarged in BOIexf compared to the bulk BiOI (0.915 nm, Figure 1j, k). This suggests that the interlayer van der Waals (vdW) forces have been reduced due to the LPE process. Since the bulk BiOI is synthesized under high pressure and temperature condition and exfoliated to nanoscale thickness, the surface tension of (001) layers can increase thus enlarging the distance between the layers.[36] Besides, amorphous layers covered the whole nanosheets of BOIexf, as shown in Figure 1f and 1i. These amorphous layers include various species during the synthesis process, which will be discussed later through X-ray photoelectron spectroscopy (XPS) analysis (Figure 2). Moreover, Raman spectra of BOI and BOIexf are shown in Figure 1l. Both samples have main peaks at around 84.9 (A1g internal Bi-I stretching mode), 109.4 (external $A_{1g}$ Bi-I stretching mode), and 152.7 $cm^{-1}$ (Eg internal Bi-I stretching mode) corresponding to the Raman active vibrational modes of tetragonal BiOI.[37] In the spectrum from BOIexf, we observe decreased intensity of the peaks of $A_{1g}$ internal Bi-I stretching mode and $E_g$ internal Bi-I stretching mode, indicating less internal Bi-I stretching modes are detected in the exfoliated sample (see a clear comparison in Figure S1). This is because the exfoliation of BiOI decreases the effective forces acting on the atoms caused by interlayer vdW interactions.[37] Moreover, a slight shift to higher frequency of all the three characteristic peaks assigned to BiOI is contradictory to the previous literature, which might result from the influence of the surface species induced during the exfoliation. Furthermore, the emergence of the peak at 117.7 $cm^{-1}$, attributed to $Bi_2O_3$, provides additional evidence for the generation of bismuth oxide species during the exfoliation process.[38]

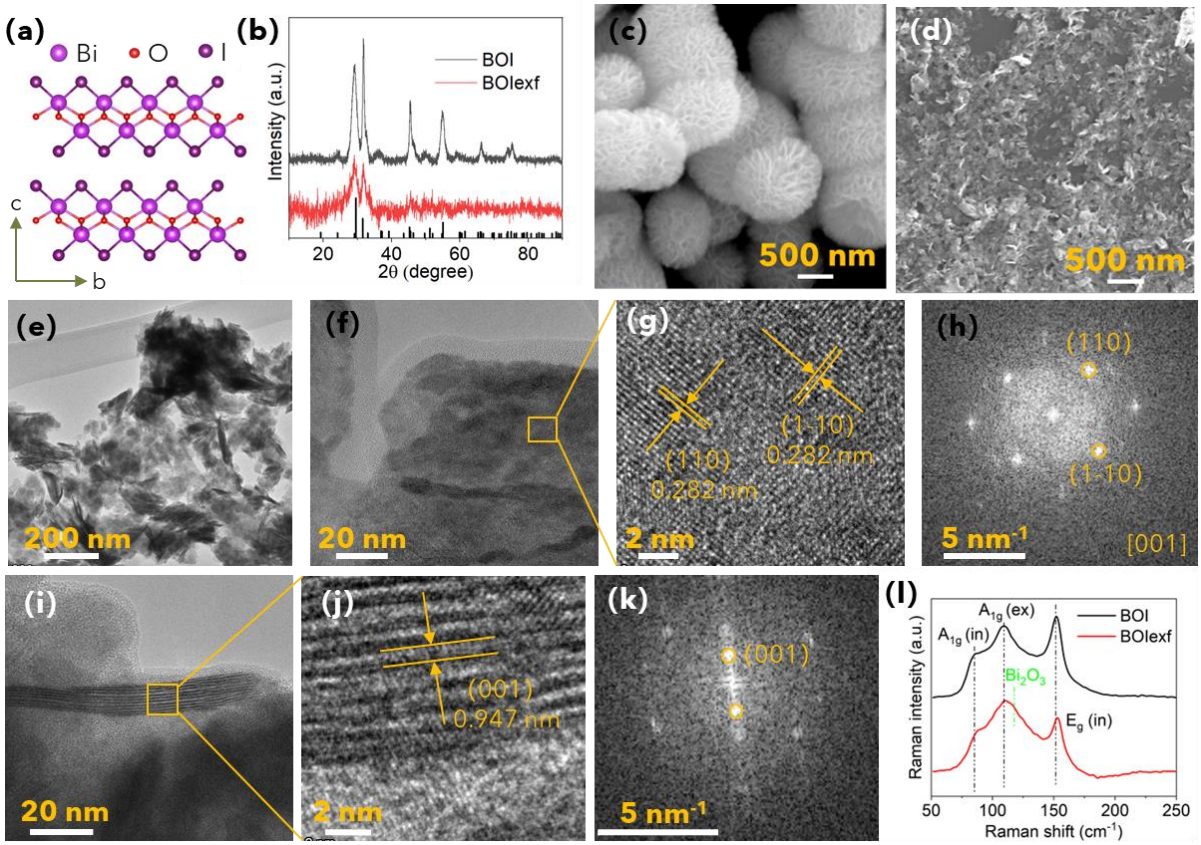


**Figure 1.** a) Crystal structure of layered BiOI; b) XRD patterns of BOI and BOIexf; SEM image of c) BOI and d) BOIexf; e) A representative TEM image of BOIexf; f) HRTEM image of the top view of the exfoliated BiOI nanosheets; g) image of the marked area in image f) and h) FFT pattern transferred from image g); i) HRTEM image of the side view of the exfoliated BiOI nanosheets; j) image of the marked area in image i) and k) FFT pattern transferred from image j; l) Raman spectra of BOI and BOIexf.

To further ascertain the surface chemical environment and surface species of the samples before and after exfoliation, XPS measurements were performed on BOI and BOIexf samples and their results are shown in Figure 2. With regard to C1s spectra, the XPS peaks at 284.8 and 287.8 eV corresponded to C-C bonds from carbon species in the XPS measurement and $CO_3^{2-}$ species from the samples.[39] The increase in the integrated area of the peak at 287.8 eV in BOIexf demonstrates an increase of $CO_3^{2-}$ species on the exfoliated BiOI sample. Figure 2b shows the Bi 4f spectra of BOI and BOIexf. The peaks for BOI and BOIexf are well divided with six peaks at their respective binding energies. The peaks of BOI at 158.7, 159.5 and 162.2 eV can be attributed to the Bi $4f_{7/2}$ in $Bi_2O_3$, $[Bi_2O_2]$ layer and $Bi^{5+}$ species, while the peaks at 164.0, 164.9 and 167.5 eV are the corresponding Bi $4f_{5/2}$ peaks of $Bi_2O_3$, $[Bi_2O_2]$ layer and $Bi^{5+}$

species.[40–43] Considering that [$Bi_2O_2$] layer can exist in BiOI, $Bi_2O_2CO_3$ and $BiOIO_3$, the peak of [$Bi_2O_2$] layer probably stands for both chemical surroundings of Bi in BiOI nanosheets and Bi inside $Bi_2O_2CO_3$/$BiOIO_3$ species. However, all these peaks for BOIexf exhibit higher binding energies compared to BOI, indicating that extra interactions in the interface among the BiOI nanosheets and surficial species exist, creating different kinds of bonds.[44] This also shows that the surface species become more oxidized during the exfoliation process. Specifically, the $Bi_2O_3$ species are consumed or converted to other Bi species during the exfoliation, as the integrated area of $Bi_2O_3$ in BOIexf is decreased dramatically compared to BOI. The I $3d_{5/2}$ peak of BOI are fitted at 618.8, 620.0, and 622.0 eV, which are attributed to the I in BiOI, $I_3^-$ and $IO_3^-$, respectively (Figure 2c).[45,46] The peaks at 630.3, 631.5 and 633.5 eV are the corresponding I $3d_{3/2}$ peaks. Versus BOI, the peaks of I 3d in BOIexf has shifts towards positive deviation. The shifts again revealed a strong interaction among the BiOI nanosheets and the species, which is in accordance with the phenomenon in Figure 2b.[44] Meanwhile, the integrated area of BiOI is decreased after LPE, indicating that the BiOI nanosheets are more covered by $I_3^-$ and $IO_3^-$ after the exfoliation (Table 1 and S1). For the O1s spectrum of BOI, the fitted peaks located at 529.2, 530.4 and 531.3 eV correspond to the O in Bi-O (including [$Bi_2O_2$] layers and $Bi_2O_3$), $IO_3^-$, $CO_3^{2-}$, while the other two peaks at 532.5 and 533.8 eV are chemically adsorbed hydroxide species and $H_2O$.[47–49] Differently from BOI, a large amount of chemically and physically adsorbed $H_2O$ was found on BOIexf.[50] This might be because the added $IO_3^-$ and $CO_3^{2-}$ can promote the adsorption of $H_2O$ chemically, and multilayers of $H_2O$ adsorbs further through hydrogen bonds on the chemically adsorbed $H_2O$.[45] To summarize the results from XPS spectra and quantify the amount of surface species in Table 1, it is clear that the surface environment is dramatically changed during the exfoliation step: keeping most kinds of species reserved on BiOI nanosheets, the amount of $CO_3^{2-}$, $IO_3^-$, $Bi^{5+}$, $I_3^-$ and hydroxide species is increased, while $Bi_2O_3$ is decreased. These $Bi_2O_3$ components are either oxidized into Bi species with higher binding energy or simply decomposed during exfoliation. Besides, an additional amount of $H_2O$ is absorbed physically on the BOIexf.

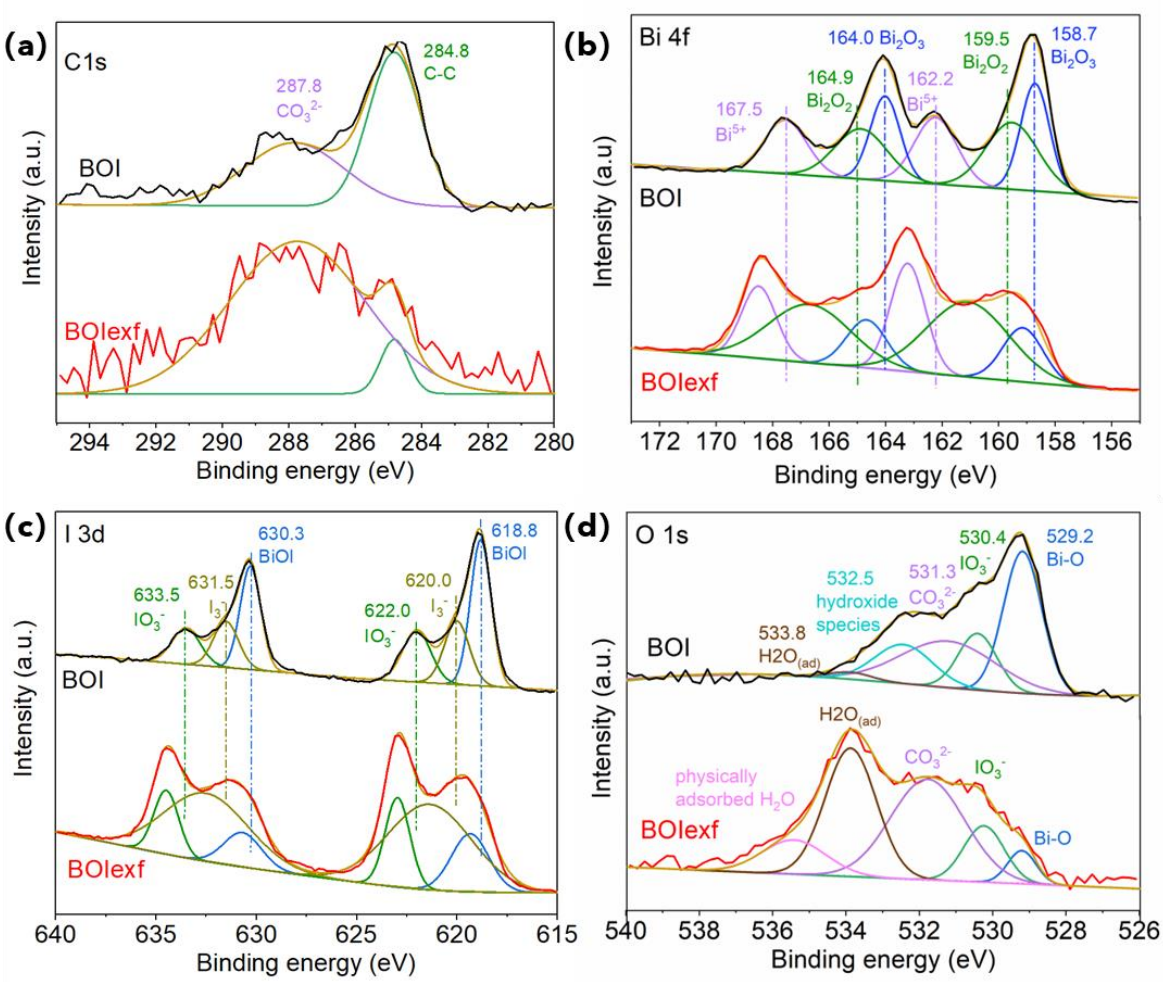


**Figure 2.** High-resolution XPS spectra of a) C 1s, b) Bi 4f, c) I 3d and d) O 1s of as-prepared samples BOI and BOIexf.

The PEC performance of the two BiOI samples was evaluated, revealing that the exfoliation process has a significant influence on the photoelectrode performance. Before detailing the impact of exfoliation on the PEC performance of the BiOI samples, UV–vis absorption spectra were collected to assess the optical properties of the photoelectrodes (Figure 3a). BOIexf exhibited a smaller absorption edge at around 520 nm than the original BOI (610 nm). The Tauc plots, which depict the computation of the optical bandgap for photoanodes, are presented in Figure 3b. BOI and BOIexf feature band gaps of 2.03 and 2.39 eV, respectively. These results demonstrate that the exfoliation process leads to a quantum confinement effect in BOI by reducing the size and thickness of BOI.[51] The PEC performance of the BiOI samples was subsequently conducted using a three-electrode system in 0.5 M $Na_2SO_4$. The powder samples were drop-casted on the FTO substrates for further PEC measurements. The linear sweep voltammetry (LSV) curves of BOI and BOIexf under chopped illumination are represented in Figure 3c. In general, both the samples display similar onset potential for OER. The

photocurrent density is 29 and 35 μA/cm$^2$ at 2.2 V vs. RHE for BOI and BOIexf, respectively. However, during the subsequent chronoamperometry (CA) test at 2.2 V vs. RHE, the photocurrent density of BOI and BOIexf significantly increases along the 5500 s irradiation time (Figure 3d). Specifically, the photocurrent of BOI increases slowly from ~13 μA/cm$^2$, and the change in photocurrent ends at around 2000 s with a value of ~34 μA/cm$^2$, while the current measured in the dark first decreases and then increases gradually to 60 μA/cm$^2$ after 5500 s. BOIexf shows a similar trend: the photocurrent increases dramatically from ~30 to ~85 μA/cm$^2$, which is more than twice larger than the bulk BiOI. Meanwhile the current in dark decreases in the first 100 s, then increases and stabilizes at around 4000 s with a value of 85 μA/cm$^2$. These changes of the current density along the irradiation time reveal a clear enhancement both in photocurrent and dark current for the exfoliated BiOI compared to the bulk BiOI. More importantly, a re-arrangement of the samples structure probably happens either in the crystal lattice or in the surface chemistry, as analyzed later in the text. The stabilized region in 5000-5500 s time range of the CA in Figure 3d is shown in Figure 3e more in detail, to better analyze the charge transfer during the PEC process. For BOIexf, the transient photocurrent response clearly indicates the effects of surface recombination. The instantaneous current observed when the light is switched on reflects the photogenerated holes reaching the surface.[52] The immediate decline towards the average photocurrent value is caused by the capture of accumulated holes in surface states, and these holes recombine then with free electrons. The current overshoot observed when the light is switched off is due to the accumulation and releasing of holes from the surface to the electrolyte, as a positive voltage is still applied on BOIexf and the trapped holes are released to electrolyte under dark environment. It should be noted that the photocurrent decays are very different between BOIexf and BOI, on which the current decay is not apparently observed when light is on, while the current gradually drops down when light is off. This suggests the different separation and recombination of photogenerated electron–hole pairs between BOI and BOIexf. For BOI, when the UV light is switched on, a small number of holes are likely trapped and recombined. The decline in photocurrent due to this recombination can offset the increased current from the charging of the double layer capacitance, resulting in the current displaying a straight line. The current drop in the dark is primarily due to the discharge of the double layer capacitance, which becomes the dominant charge behavior.

The electrochemical surface area (ECSA) of the samples were analyzed using cyclic voltammetry plots to further characterize the PEC properties of the samples. The estimated active area is 35.62 and 0.54 μF/cm$^2$ for BOIexf and BOI photoelectrodes, respectively (Figure

3g). Compared to the original ECSA (0.91 and 0.55 μF/cm$^2$ for BOIexf and BOI, respectively, see Figure S2), the active sites of BOIexf was increased by ~40 times after a long-term CA stabilization, while the ECSA of BOI shows no apparent modification. Therefore, we can safely state that during this stabilization, the active sites on BOIexf are increased, and thus current density of BOIexf increases gradually. Electrochemical impedance spectroscopy (EIS) Nyquist plots were further performed to investigate the charge transfer process. As shown in Figure 3g, a smaller radius of the arc is observed on BOIexf compared to BOI, indicating the smallest charge transfer resistance of BOIexf. Besides, to compare the resistance of the samples before OER, it is apparent that the resistance of BOIexf is dramatically reduced during the OER measurement, which can be considered as one of the reasons why PEC OER of BOIexf is enhanced (Figure S3).

To further discuss the discrepancy in PEC performance between the two samples, the transient open circuit potential (OCP) characterization was carried out and the results are shown in Figure 3h, from which the photovoltage could be obtained from the difference in the steady-state voltage in dark and under illumination. Both the as-prepared electrodes show a negative increase in voltage under light irradiation, indicating the photogenerated electrons are injected from the BiOI into the FTO substrate, and the photoanode acts as an n-type semiconductor material.[53] It is clear that the photovoltage for BOIexf (64 mV) is significantly lower than that of BOI (37 mV), indicating the higher photogenerated electron density in BOIexf under illumination and better free charge production ability of BOIexf. When comparing the photovoltage of the samples before OER in Figure S4, it is evident that the photovoltage of both BOI and BOIexf increases. This indicates that the CA process also enhances their ability to separate photogenerated charges.[54]

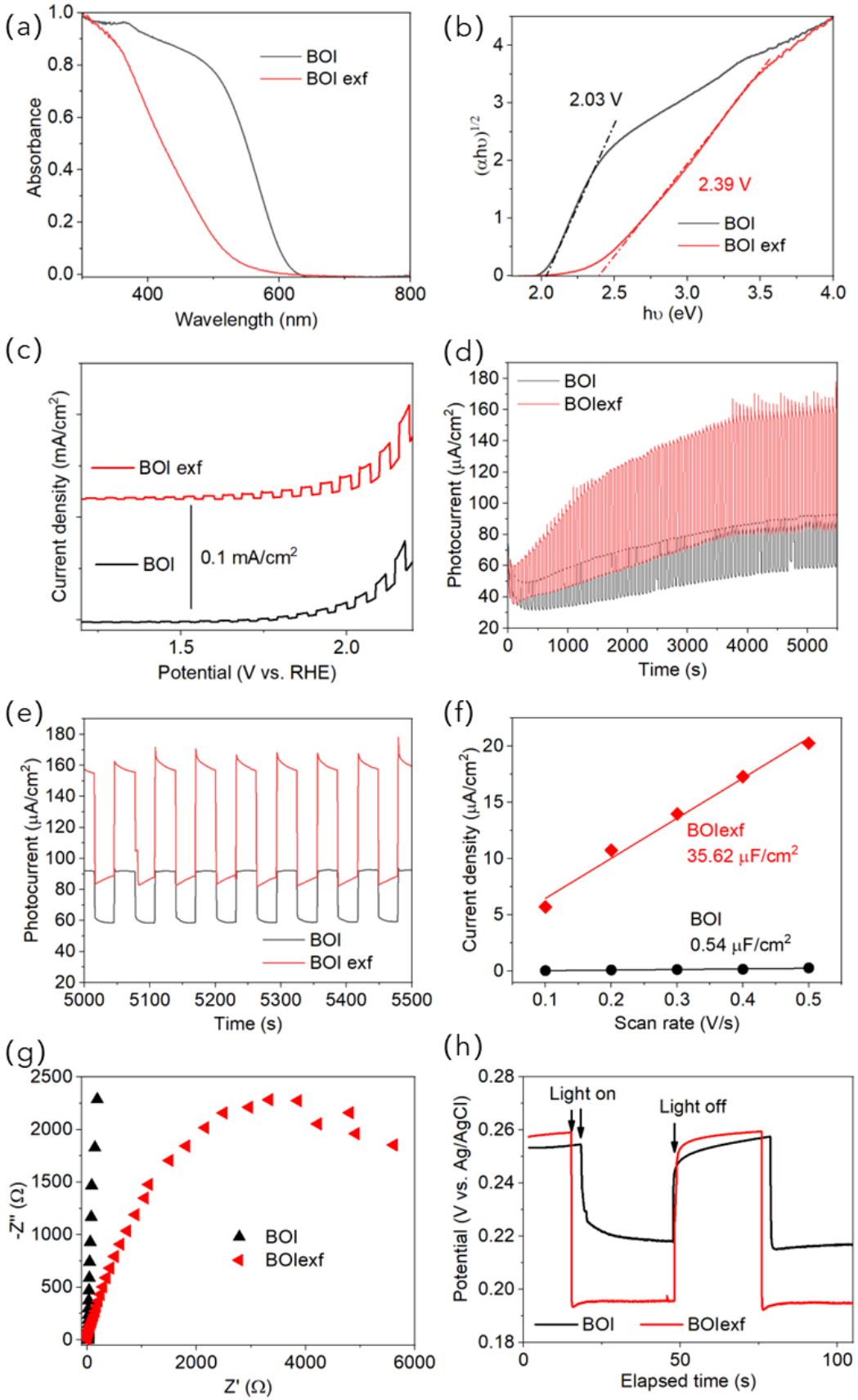


**Figure 3.** a) UV–vis spectra; b) Tauc plots; c) LSV curves; d) long-term CA recorded at 2.2 V versus RHE of BOI and BOIexf; e) is the magnification of image d); f) estimated ECSA; g) EIS plots and h) OCP decay profiles of BOI and BOIexf after the long-term CA test.

To understand further what brings the modification of the PEC performance after a long-term CA test for the two samples, these were collected and analyzed after the PEC test. As shown in Figure S5, both BOI and BOIexf photoelectrodes on FTO exhibit clear diffraction peaks which can be assigned to tetragonal BiOI (ICSD No. 391354). Further morphology and structural analysis by TEM and HRTEM were performed on BOIexf collected after PEC OER measurement. As shown in Figure 4a and 4b, the layered morphology is sustained during the OER. The FFT (Figure 4d) converted from Figure 4c verifies that these layers belong to tetragonal BiOI (ICSD No. 391354), which is in accordance with the XRD patterns. The fringe lattice analysis of the side view of the layers shows that these layers are (001) nanosheets, and the layer distance shrinks to the standard (003) layer distance of 0.305 nm. This is clear evidence that the surface tension is decreased to the natural level and BOIexf layers is stabilized during the long-term CA. Compared to the HRTEM images in Figure 1e and 1h, the amorphous layer covered on BOIexf is not displayed in Figure 4b, meaning that the amorphous surface species are probably consumed during the PEC OER. Following the PEC test, we analyzed the UV-vis absorption spectra and calculated the band gap of the two samples using Tauc plots, as shown in Figure S6. The band gap values for BOI and BOIexf were determined to be 2.00 eV and 2.29 eV, respectively. These values are lower than the band gaps measured before the PEC reactions, suggesting that the PEC process may cause sintering of the nanomaterials, making their properties more similar to bulk BiOI. Additionally, the absorption spectrum exhibited noticeable fringes, which are attributed to the FTO film located between the glass substrate and the BiOI thin films.[55]

XPS measurement of BOI and BOIexf after PEC OER further illustrates that the species on both the samples have changed during the CA stabilization process. C 1s spectra in Figure S7a can be fitted into 2 peaks, which are assigned to environmental C-C (284.8 eV) and $CO_3^{2-}$ species (286.8 eV). This decrease of binding energy of $CO_3^{2-}$ species compared to the samples before OER indicates that the oxidation state of C decreases during the reaction. The ratios of $CO_3^{2-}$ of before and after OER are roughly compared in Table 1. Surprisingly, the ratio of $CO_3^{2-}$ is adjusted to around 61% in both samples, though they have very different $CO_3^{2-}$ ratios before OER (see Figure 2a and Table 1). This consequent unity of $CO_3^{2-}$ ratio might be related to the pH, dissolved $CO_2$ in the electrolyte and anodic potential. The binding energy (Figure 4f) at about 164.4 and 159.1 eV can be attributed to Bi $4f_{5/2}$ and $4f_{7/2}$ in $[Bi_2O_2]$ layers respectively. Similarly, the binding energy at about 161.1 and 166.3 eV are ascribed to Bi $4f_{5/2}$ and $4f_{7/2}$ of $Bi^{5+}$, respectively. It should be noticed that the binding energy of $Bi^{5+}$ is less in BOIexf than in

BOI, which indicates that the oxidation state is slightly reduced in BOIexf. However, compared to the Bi 4f spectra of the samples before PEC OER, it is apparent that $Bi_2O_3$ species, which has a lower binding energy compared to other Bi species, are largely consumed during the OER, since no apparent peaks related to $Bi_2O_3$ are detected in Figure 4f. Additionally, all the characteristic peaks in Figure 4e are shifted to the low binding energy direction compared to the corresponding peaks in Figure 2a. This suggests that the initial extra species that caused additional interactions are eliminated, and the surface of BiOI samples is stabilized in an intermediate oxidized state. The resulting Bi 4f spectra appear cleaner than the spectra before PEC OER, indicating a possible stabilization to a stable surface state during the reaction as well. In BOI, the binding energies of I $3d_{5/2}$ and I $3d_{3/2}$ are 619.0 and 630.4 eV for chemical environment around I inside BiOI, 621.0 and 632.2 eV for $I_3^-$ species, and 624.0 and 635.6 eV for $IO_3^-$ species, respectively (Figure 4g). The fitted peaks of $I_3^-$ from BOIexf also shifts to lower binding energy, which agrees with the spectra of Bi 4f in Figure 4f. However, there is no signal of $IO_3^-$ detected inside BOIexf, meaning that $IO_3^-$ species are consumed during CA. Additionally, the fitting of spectra of O 1s have shown the existence of H-O, C-O, I-O and Bi-O in BOI, and H-O, C-O and Bi-O for BOIexf (Figure S7b). Table 1 summarizes the changes in the amounts of surface species. Notably, $I_3^-$ reaches an equilibrium ratio of approximately 32% after CA. This equilibrium indicates that $I_3^-$ can be reversibly converted from $I^-$, with the ~32% value representing the balance among all surface I elements. Additionally, the increase in hydroxide species suggests improved adsorption ability of intermediates for the OER, indicating that the samples exhibit enhanced potential for OER after CA.

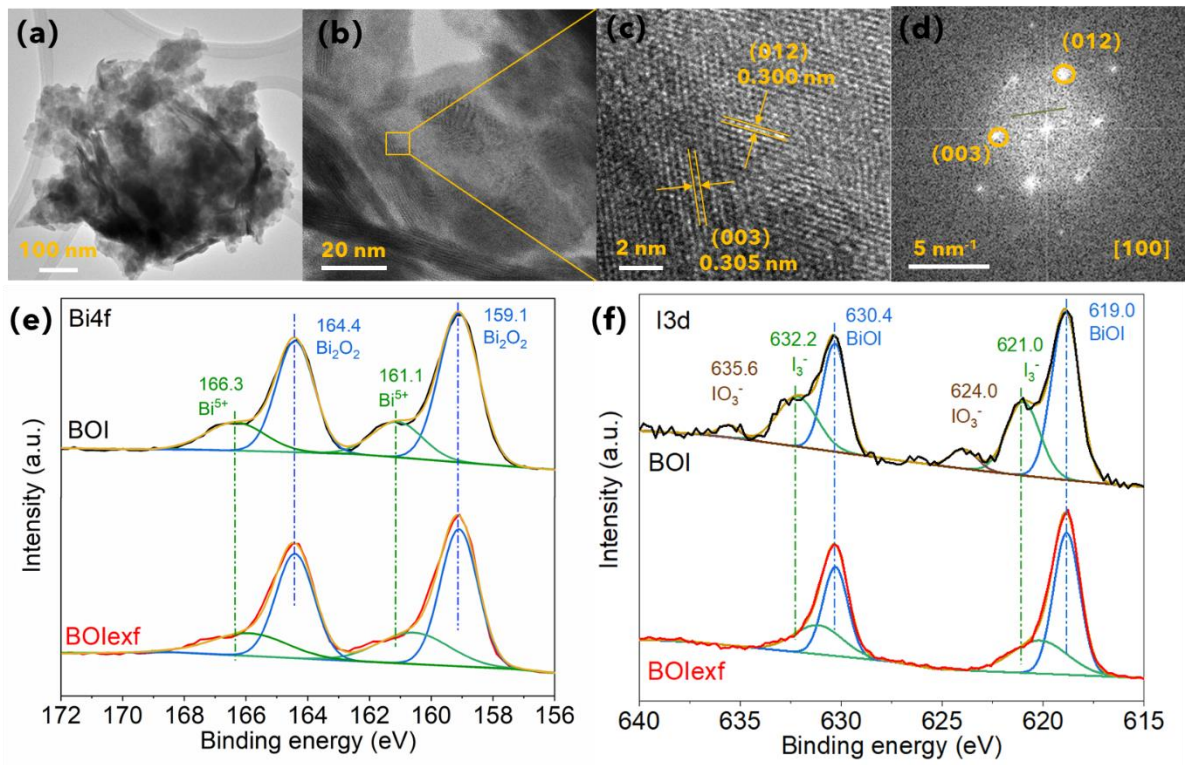


**Figure 4.** a) TEM and b) HRTEM images of BOIexf after PEC OER; c) image of the marked area in image b) and d) FFT pattern transferred from image d); High-resolution XPS spectra of e) Bi 4f and f) I 3d of BOI and BOIexf after PEC OER.

**Table 1.** Ratio changes of surface species on BOI and BOIexf before and after anodic PEC CA.

| | **BOI** | | **BOIexf** | |
|---|---|---|---|---|
| **Species** | **Before** | **After** | **Before** | **After** |
| $CO_3^{2-}$ [a)] | 43.8% | 63.0% | 93.2% | 60.5% |
| $Bi^{5+}$ [b)] | 30.3% | 23.1% | 29.4% | 30.3% |
| $Bi_2O_3$ [c)] | 33.4% | 0 | 19.3% | 0 |
| $IO_3^-$ [d)] | 23.8% | 6.7% | 18.8% | 0 |
| $I_3^-$ [e)] | 26.5% | 32.1% | 64.0% | 32.9% |
| Hydroxide species[f)] | 17.5% | 56.2% | 45.0% | 60.0% |

[a)] Calculated based on C 1s spectra, atomic ratio of C in $CO_3^{2-}$ / all the surface C element; [b)] Calculated based on Bi 4f spectra, atomic ratio of Bi as $Bi^{5+}$ / all the surface Bi element; [c)] Calculated based on Bi 4f spectra, atomic ratio of Bi in $Bi_2O_3$ / all the surface Bi element; [d)] Calculated based on I 3d spectra, atomic ratio of I in $IO_3^-$ / all

the surface I element; [e)] Calculated based on I 3d spectra, atomic ratio of I in $I_3^-$ / all the surface I element; [f)] Calculated based on O 1s spectra, atomic ratio of O in all the hydroxide species / all the surface O element.

Based on the above measurements and analysis, we can hypothesize a mechanism explaining how species present on the surface of BiOI and the PEC OER performance of the material influence each other. According to the analysis of XPS spectra before and after CA, it straightforwardly emerges that the type and ratios of surface species on the oxyhalide samples change during prolonged photoelectrode operation. Figure 5a displays the chemical reactions that happened on the surface of the BOI photoanodes. Behaving as the photoanode, the holes from both light and positive bias will diffuse into the electrolyte and create an acidic microenvironment in the neutral electrolyte. This richness of protons near the surface of BOI promotes the dissolution of $Bi_2O_3$ and the combination of $[Bi_2O_2]$ layers and $H_2CO_3$ to form $Bi_2O_2CO_3$ (Table 1). Also, some $I^-$ can absorb the holes and form $I_3^-$. On the other side, most of the photogenerated electrons will migrate to the FTO substrate and then to the cathode. However, there will be still some electrons flowing to $Bi^{5+}$ and $IO_3^-$ to reduce them into $Bi^{3+}$ and $I^-$. The chemical reactions of the surface species on BOIexf differ from those on BOI during the initial period of CA, primarily in terms of $I_3^-$ and $Bi_2O_2CO_3$ distribution. Due to the initial high levels of $I_3^-$ (64% of all I elements) and $Bi_2O_2CO_3$ (93.2% of all carbon elements) on BOIexf, which exceed their equilibrium ratios (26.5% for $I_3^-$ and ~61% for $Bi_2O_2CO_3$), the $I_3^-$ on BOIexf is reduced to $I^-$, while the excess $Bi_2O_2CO_3$ dissolves into the electrolyte (Table 1 and Table S1 and S2 for calculation details). These adjustments in surface species likely occur during the initial period, coinciding with the decrease in current observed in Figure 5b and 5d for BOI and BOIexf, respectively, as these reactions irreversibly consume charges. By comparing the photocurrent response in Figure 5b and 5d, it is evident that BOIexf reaches equilibrium in around 150 seconds, indicated by the increase in current after this period. In contrast, BOI completes the tuning of its species in approximately 600 seconds. Given that exfoliation does not increase the ECSA of the samples (Figure S2) but does increase the number of surface species, we speculate that these thicker layers may more readily be consumed or converted to active sites for absorbing charges, subsequently increasing the ECSA and improving the resistance of the system (Figure 3f and 3g).

After the samples reach the balance of different surface species, the current is stabilized (Figure 3e). The surface species are in a dynamic state, as shown in Figure 5e. Specifically, the pairs $Bi_2O_2CO_3$ / $[Bi_2O_2]^{2+}$, $IO_3^-$ / $I^-$, $I_3^-$ / $I^-$, and $Bi^{3+}$ / $Bi^{5+}$ can interconvert reversibly. Interestingly, the ESCA of BOIexf is increased by 40 times after CA while the photocurrent obtains a

modification of ~2.5 times, meaning that the intrinsic OER activity of BOIexf is not modified, which is further proved by the ECSA-normalized photocurrent density of BOI and BOIexf (Figure S8).[56] This might be because surface $Bi^{5+}$ and $I_3^-$ species on BOI have higher binding energy than those on BOIexf, which means that a better quality interface forms between these species and the BiOI, with consequent improved charge separation and transfer on each active site.[44,57] Moreover, the residual $IO_3^-$ is helpful to increase the efficiency of charge separation and transfer in BOI as well.[35]

Based on the above analysis, it is clear that the exfoliation process reduces the size of the BOI nanosheets and generally increases the number of surface species. However, this step does not directly enhance the active sites for PEC OER. Under high positive voltage and light, the numerous surface species on the exfoliated BiOI are consumed or converted in a short time, creating more active sites and decreasing the resistance, thereby improving the OER performance. Nonetheless, the intrinsic PEC activity is higher in BiOI before exfoliation due to the presence of $IO_3^-$ groups and a stronger connection between $Bi^{5+}$ and $I_3^-$.[45]

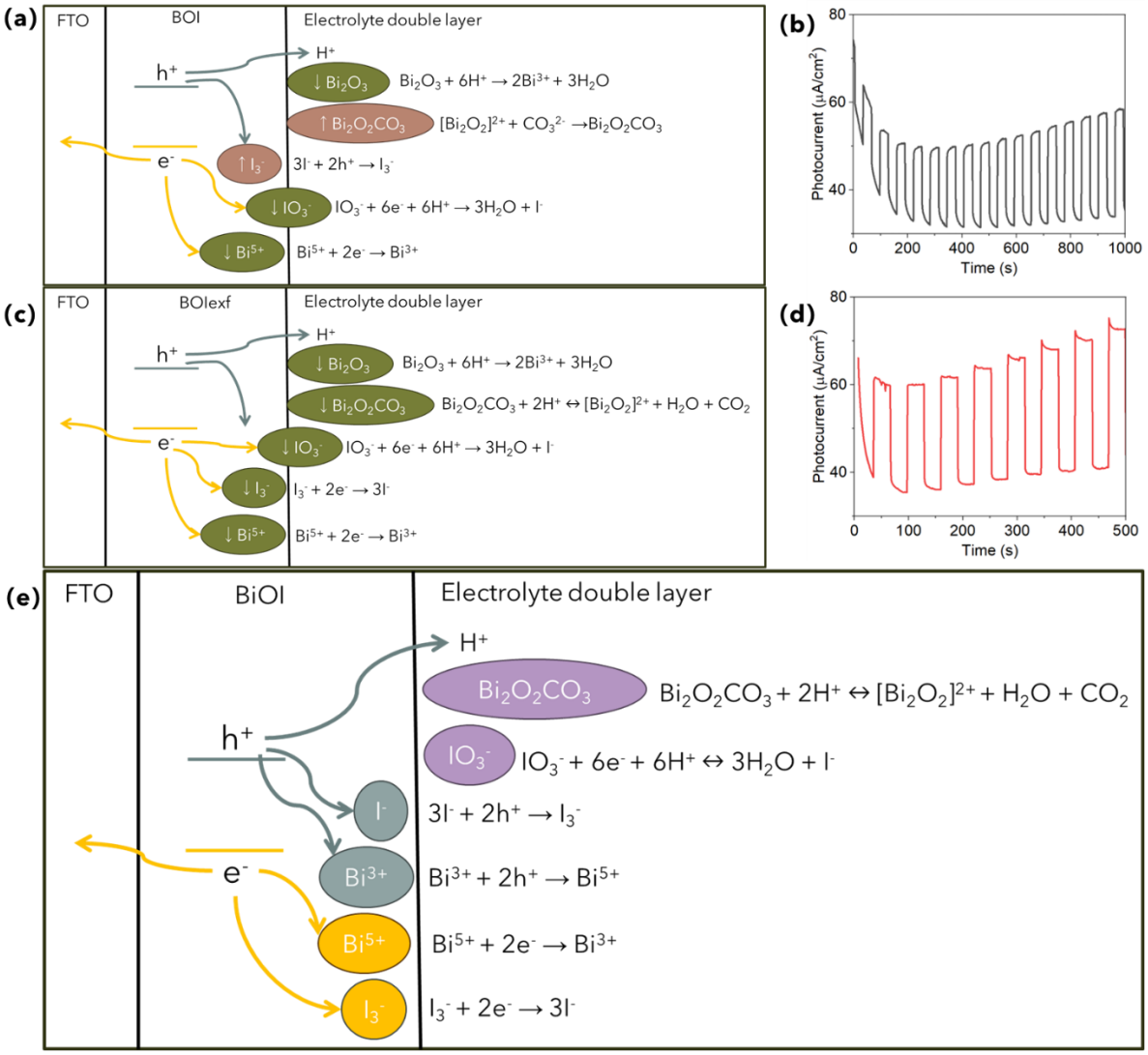

**Figure 5.** a) Chemical reactions happening at the surface and b) photocurrent responses of BOI during the initial period of PEC OER CA; c) Chemical reactions happening on the surface and d) photocurrent responses of BOIexf during the initial period of PEC OER CA; e) Balanced chemical reactions happening on BOI and BOIexf after the samples are stabilized during prolonged PEC OER CA.

## 3. Conclusion

In summary, two types of BiOI photoelectrocatalysts were prepared by microwave method and further LPE. It is found that by using ethylene glycol as the solvent during the synthesis, surface active species including $Bi_2O_3$, $IO_3^-$, $I_3^-$, $CO_3^{2-}$, $Bi^{5+}$ and various hydroxides are existing on the on BiOI in both cases. After an additional exfoliation step, the quantity of these species increases overall, and their mutual interactions and with the BiOI matrix becomes tighter. These enhanced surface species, with improved connections on BiOI, are crucial for increasing the electrochemical surface area and reducing resistance, thereby enhancing the PEC OER performance. However, the intrinsic PEC activity remains superior in BiOI before exfoliation, likely due to the presence of $IO_3^-$ groups and a stronger connection between $Bi^{5+}$ and $I_3^-$.

This study introduces straightforward, energy-efficient and potentially scalable methods to enhance the PEC properties of BiOI layered materials by using a combination of microwave treatment and LPE. Additionally, it provides new valuable insights into the surface chemistry of these materials and its impact on PEC performance, offering a foundation for fine-tuning other 2D layered photoelectrocatalysts.

## 4. Experimental Section

*Chemicals*: Bismuth(III) nitrate pentahydrate ($Bi(NO_3)_3{\cdot}5H2O$), potassium iodide (KI), ethylene glycol (EG), isoproponal, ethanol and fluorine-doped tin oxide (FTO) coated glass substrates were purchased from Sigma-Aldrich. Milli-Q water used in all the experiments was obtained using the Milli-Q ultrapure system.

*Preparation of photoelectrocatalysts*: $Bi(NO_3)_3{\cdot}5H_2O$ and KI were used as precursors to successfully synthesize BiOI microspheres by a microwave reaction, which is modified from the previous work of Reyna-Cavazos et al.[58] Briefly, 0.1 M KI and 0.1 M $Bi(NO_3)_3{\cdot}5H_2O$ solutions in EG were prepared separately. Then 10 mL of each solution was added to a microwave vial of 30 mL with a stirring bar. The microwave reaction is operated in a Monowave200 microwave reactor, and 5 min is set to raise the temperature from room temperature to 135 °C. The reaction time continued for 35 min at 135 °C. After cooling to 50 °C,

the orange sample was collected and washed with ethanol and $H_2O$ to remove unreacted chemicals and impurities.

To synthesize exfoliated BiOI (BOIexf), the as-prepared BiOI microsphere was first dried under vacuum, then 0.5 g of BiOI powder was dispersed in 50 mL of isopropanol for further LPE. After 9 h of tip-sonication, the mixture was centrifuged at 2000 rpm for 5 min to get rid of the unexfoliated particles, and a stable colloidal suspension was obtained. Then, the suspension was centrifuged at higher speed of 8000 rpm for 10 min to obtain BOIexf.

*Characterization:* XRD was performed using a Panalytical X'Pert PRO diffractometer with a Cu Kα source (40 kV, 40 mA). SEM was conducted with a Carl Zeiss electron microscope at an acceleration voltage of 3 kV and a current of 100 pA. TEM and HRTEM imaging were performed on a TALOS F200X (ThermoScientific, Eindhoven, Netherlands) instrument without aberration correction, operating at an acceleration voltage of 200 kV. Images were captured using a 16-megapixel CMOS camera, and the fast Fourier transform (FFT) pattern was processed with Velox software (Thermo Scientific Velox Software, Thermo Fisher Scientific Inc., Waltham, MA, USA). Samples were prepared by dropping dilute suspensions of nanomaterials in ethanol onto carbon film-coated 200 mesh copper grids. Raman spectra were recorded using a Senterra spectrometer from Bruker Optics with OPUS 7.5 software, employing a 532 nm excitation laser. Concentrated samples were drop-cast onto glass and measured with 80 co-additions and 25 seconds of integration time. XPS spectra were recorded on a PHI 5000 VersaProbe II spectrometer from Physical Electronics GmbH. UV-vis absorption spectra of BiOI suspensions were obtained using a Goebel Uvikon spectrometer with a quartz cuvette having an optical path length of 1 cm. The spectra were recorded from 300 to 800 nm with a scan interval of 0.25 nm. Optical absorption properties of BiOI films on FTO electrodes were characterized using a UV-vis-NIR Spectrometer (Jasco V-770) with a scan resolution of 1 nm. One halogen lamp, one deuterium lamp and the peltier cooled PbS detector were equipped on the spectrometer. Thin film absorption and transmission spectra were acquired using an integrating sphere attached to the spectrophotometer. Baseline acquisition was conducted with the integrating sphere with FTO.

*Photoelectrochemical measurements:* PEC OER tests were performed using a photoelectro-chemical reaction cell with three electrodes in a 0.5 M $Na_2SO_4$ electrolyte medium. The reference electrode is Ag/AgCl (saturated KCl electrolyte) and the counter electrode is a platinum wire. For the PEC OER experiments, all the samples were dried in air and dispersed again in ethanol at a concentration of 5mg/mL, and the inks were dropping cast on conductive FTO glass. A mercury lamp with a light intensity of 16 mW/cm2 was used as a light source.

The potentiostatic test was conducted on an Autolab instrument, and LSV was performed at a scan rate of 10 mV/s in the range of 1.1 to 2.2 V vs. RHE. The transient photocurrent measurements were examined at 2.2 V vs. RHE during four on/off light cycles. EIS measurements were performed under light irradiation at 1.23 V (vs. RHE) with the frequency range being adjusted between 100 kHz and 0.1 Hz. ECSA was calculated by recording cyclic voltammograms for 10 cycles between 0.8 and 1.0 V vs. RHE at different scan rates of 0.1, 0.2, 0.3, 0.4 and 0.5 V/s.

**Supporting Information**

Supporting Information is available from the Wiley Online Library or from the author.

**Acknowledgements**

T.G. acknowledges the support of the European Research Council for the project JANUS BI (grant agreement no. [101041229]). M.W. and T.G. also thank Fondazione Compagnia di San Paolo for financial support through the "Bando TRAPEZIO - Paving the way to research excellence and talent attraction". T.G. is also further grateful to Fondazione Compagnia di San Paolo for the support through the Starting Grant ERC program.

**References**

[1] Z. Sun, T. Amrillah, *Nanoscale* **2024**, *16*, 5079.

[2] M. Wang, M. Langer, R. Altieri, M. Crisci, S. Osella, T. Gatti, *ACS Nano* **2024**, *18*, 9245.

[3] K. Dou, C. Peng, R. Wang, H. Cao, C. Yao, J. Qiu, J. Liu, N. Tsidaeva, W. Wang, *Chem. Eng. J.* **2023**, *455*, 140813.

[4] B. O. Orimolade, B. A. Koiki, G. M. Peleyeju, O. A. Arotiba, *Electrochim. Acta* **2019**, *307*, 285.

[5] C. T. Haile, N. Ahmad, C. W. Chiu, C. F. Jeffrey Kuo, *Chemosphere* **2023**, *323*, 138108.

[6] Y. Gao, S. Zhang, X. Bu, Y. Tian, *Catal. Today* **2019**, *327*, 271.

[7] R. Xu, D. Zhu, K. Du, D. Cui, H. Feng, W. Hao, D. Tian, Y. Du, *Mater. Today Energy* **2022**, *25*, 100961.

[8] Y. Wang, M. Zu, X. Zhou, H. Lin, F. Peng, S. Zhang, *Chem. Eng. J.* **2020**, *381*, 122605.

[9] A. M. Chang, Y. H. Chen, C. C. Lai, Y. C. Pu, *ACS Appl. Mater. Interfaces* **2021**, *13*, 5721.

[10] N. T. Hahn, S. Hoang, J. L. Self, C. B. Mullins, *ACS Nano* **2012**, *6*, 7712.

[11] H. Wang, Y. Liang, L. Liu, J. Hu, P. Wu, W. Cui, *Appl. Catal. B Environ.* **2017**, *208*, 22.

[12] R. Tan, A. Sivanantham, B. Jansi Rani, Y. J. Jeong, I. S. Cho, *Coord. Chem. Rev.* **2023**, *494*, 215362.

[13] X. Sun, J. Wu, Q. Liu, F. Tian, *Appl. Surf. Sci.* **2018**, *455*, 864.

[14] P. Velusamy, X. Liu, M. Sathiya, N. S. Alsaiari, F. M. Alzahrani, M. T. Nazir, E. Elamurugu, M. S. Pandian, F. Zhang, *Chemosphere* **2023**, *321*, 138007.

[15] S. Li, J. Liu, X. Liu, K. Yan, J. Zhang, *Electrochim. Acta* **2024**, *484*, 144058.

[16] M. Sun, J. Hu, C. Zhai, M. Zhu, J. Pan, *ACS Appl. Mater. Interfaces* **2017**, *9*, 13223.

[17] F. Zhan, G. Wen, R. Li, C. Feng, Y. Liu, Y. Liu, M. Zhu, Y. Zheng, Y. Zhao, P. La, *Phys. Chem. Chem. Phys.* **2024**, *26*, 11182.

[18] H. Wang, M. Gu, M. Yan, X. Wu, Y. Dong, G. L. Wang, *J. Mater. Chem. B* **2023**, *11*, 5123.

[19] Y. Bai, H. Bai, K. Qu, F. Wang, P. Guan, D. Xu, W. Fan, W. Shi, *Chem. Eng. J.* **2019**, *362*, 349.

[20] L. Zeng, F. Zhe, Y. Wang, Q. Zhang, X. Zhao, X. Hu, Y. Wu, Y. He, *J. Colloid Interface Sci.* **2019**, *539*, 563.

[21] H. Liu, C. Yang, J. Huang, J. Chen, J. Zhong, J. Li, *Inorg. Chem. Commun.* **2020**, *113*, 107806.

[22] J. Di, J. Xia, S. Yin, H. Xu, L. Xu, Y. Xu, M. He, H. Li, *J. Mater. Chem. A* **2014**, *2*, 5340.

[23] H. Liu, W. Cao, Y. Su, Y. Wang, X. Wang, *Appl. Catal. B Environ.* **2012**, *111–112*, 271.

[24] Y. Huang, H. Li, W. Fan, F. Zhao, W. Qiu, H. Ji, Y. Tong, *ACS Appl. Mater. Interfaces* **2016**, *8*, 27859.

[25] G. Zhang, L. Cai, Y. Zhang, Y. Wei, *Chem. – A Eur. J.* **2018**, *24*, 7434.

[26] L. Liang, J. Cao, H. Lin, X. Guo, M. Zhang, S. Chen, *Appl. Surf. Sci.* **2017**, *414*, 365.

[27] P. J. Mafa, A. T. Kuvarega, B. B. Mamba, B. Ntsendwana, *Appl. Surf. Sci.* **2019**, *483*, 506.

[28] M. Karimi-Nazarabad, H. Azizi-Toupkanloo, H. S. Sajjadizadeh, E. K. Goharshadi, M. Namayandeh Jorabchi, *Electrochim. Acta* **2024**, *491*, 144299.

[29] Y. Du, R. Ma, L. Wang, J. Qian, Q. Wang, *Sci. Total Environ.* **2022**, *838*, 156166.

[30] L. Yang, R. Wang, N. Zhou, L. Jiang, H. Liu, Q. He, C. Deng, D. Chu, M. Zhang, Z.

Sun, *Appl. Surf. Sci.* **2022**, *601*, 154277.

[31] H. Azizi-Toupkanloo, M. Karimi-Nazarabad, M. Eftekhari, A. Beshkani, *Int. J. Hydrogen Energy* **2024**, *57*, 379.

[32] K. H. Ye, Z. Chai, J. Gu, X. Yu, C. Zhao, Y. Zhang, W. Mai, *Nano Energy* **2015**, *18*, 222.

[33] Q. Ni, X. Ke, W. Qian, Z. Yan, J. Luan, W. Liu, *Appl. Catal. B Environ.* **2024**, *340*, 123226.

[34] Mengjiao Wang, Silvio Osella, Rosaria Brescia, Zheming Liu, Jaime Gallego, Mattia Cattelan, Matteo Crisci, Stefano Agnoli, Teresa Gatti, *Nanoscale* **2023**, *15*, 522.

[35] J. Xie, Y. Cao, J. Hu, Y. Tang, D. Jia, *Green Chem.* **2020**, *22*, 1424.

[36] L. Ye, H. Wang, X. Jin, Y. Su, D. Wang, H. Xie, X. Liu, X. Liu, *Sol. Energy Mater. Sol. Cells* **2016**, *144*, 732.

[37] W. Zeng, J. Li, L. Feng, H. Pan, X. Zhang, H. Sun, Z. Liu, W. Zeng, L. P. Feng, H. X. Pan, X. D. Zhang, H. Q. Sun, Z. T. Liu, J. Li, *Adv. Funct. Mater.* **2019**, *29*, 1900129.

[38] Y. Xia, Z. He, W. Yang, al -, Z. Jiang, L. Chen, N. Shi, H. Nie, Z. Liu, B. Kong, J. F. Florez-Rios, M. A. Santana-Aranda, J. G. Quiñones-Galván, A. Escobedo-Morales, A. Chávez-Chávez, A. Pérez-Centeno, *Mater. Res. Express* **2020**, *7*, 015912.

[39] G. Liu, Y. Huang, H. Lv, H. Wang, Y. Zeng, M. Yuan, Q. Meng, C. Wang, *Appl. Catal. B Environ.* **2021**, *284*, 119683.

[40] X. Sun, J. Wu, Q. Li, Q. Liu, Y. Qi, L. You, Z. Ji, P. He, P. Sheng, J. Ren, W. Zhang, J. Lu, J. Zhang, *Appl. Catal. B Environ.* **2017**, *218*, 80.

[41] Y. Cong, Y. Ji, Y. Ge, H. Jin, Y. Zhang, Q. Wang, *Chem. Eng. J.* **2017**, *307*, 572.

[42] P. Chen, H. Liu, Y. Sun, J. Li, W. Cui, L. Wang, W. Zhang, X. Yuan, Z. Wang, Y. Zhang, F. Dong, *Appl. Catal. B Environ.* **2020**, *264*, 118545.

[43] Q. Wu, S. Chai, H. Yang, Z. Gao, R. Zhang, L. Wang, L. Kang, *Sep. Purif. Technol.* **2020**, *253*, 117388.

[44] Y. Peng, H. Qian, N. Zhao, Y. Li, *Catalysts* **2021**, *11*, 1284.

[45] C. Zeng, H. Huang, F. Dong, L. Ye, T. Zhang, Y. Zhang, Y. Guo, C. Liu, Y. Hu, *Appl. Catal. B Environ.* **2017**, *200*, 620.

[46] P. Li, X. Li, Y. Guo, C. Li, Y. Hou, H. Cui, R. Zhang, Z. Huang, Y. Zhao, Q. Li, B. Dong, C. Zhi, P. Li, X. Li, Y. Guo, C. Li, Y. Hou, H. Cui, R. Zhang, Z. Huang, Y. Zhao, Q. Li, C. Zhi, B. Dong, *Adv. Energy Mater.* **2022**, *12*, 2103648.

[47] X. Guo, C. Liu, W. Hu, Z. Xu, L. Lu, C. Gao, X. Li, *Colloids Surfaces A Physicochem. Eng. Asp.* **2024**, *685*, 133333.

[48] J. Bai, Y. Li, P. Wei, J. Liu, W. Chen, L. Liu, J. Bai, Y. Li, P. Wei, W. Chen, L. Liu, J. Liu, *Small* **2019**, *15*, 1900020.

[49] B. H. Graimed, Z. H. Jabbar, M. M. Alsunbuli, S. H. Ammar, A. G. Taher, *Environ. Res.* **2024**, *243*, 117854.

[50] H. S. Casalongue, S. Kaya, V. Viswanathan, D. J. Miller, D. Friebel, H. A. Hansen, J. K. Nørskov, A. Nilsson, H. Ogasawara, *Nat. Commun. 2013 41* **2013**, *4*, 1.

[51] Z. Y. Zhao, W. W. Dai, *Inorg. Chem.* **2015**, *54*, 10732.

[52] L. M. Peter, A. B. Walker, T. Bein, A. G. Hufnagel, I. Kondofersky, *J. Electroanal. Chem.* **2020**, *872*, 114234.

[53] L. Li, H. Zhang, C. Liu, P. Liang, N. Mitsuzaki, Z. Chen, *J. Mater. Sci.* **2019**, *54*, 659.

[54] R. P. Antony, T. Baikie, S. Y. Chiam, Y. Ren, R. R. Prabhakar, S. K. Batabyal, S. C. J. Loo, J. Barber, L. H. Wong, *Appl. Catal. A Gen.* **2016**, *526*, 21.

[55] M. Pozzati, F. Boll, M. Crisci, S. Domenici, F. Scotognella, B. Smarsly, T. Gatti, M. Wang, *Colloids and Interfaces* **2024**, *8*, 28.

[56] M. Wang, Z. Dang, M. Prato, U. Petralanda, I. Infante, D. V. Shinde, L. De Trizio, L. Manna, *ACS Appl. Nano Mater.* **2019**, *2*, 5695.

[57] A. Kumar, G. Sharma, A. Kumari, C. Guo, M. Naushad, D. V. N. Vo, J. Iqbal, F. J. Stadler, *Appl. Catal. B Environ.* **2021**, *284*, 119808.

[58] K. A. Reyna-Cavazos, A. M. de la Cruz, F. E. Longoria Rodríguez, E. López-Cuellar, *Res. Chem. Intermed.* **2020**, *46*, 923.

M. Wang,* J. Gallego, M. Pozzati, and T. Gatti*

**Tuning Surface Chemistry in 2D Layered BiOI by Facile Liquid-phase Exfoliation for Enhanced Photoelectrocatalytic |Oxygen Evolution**

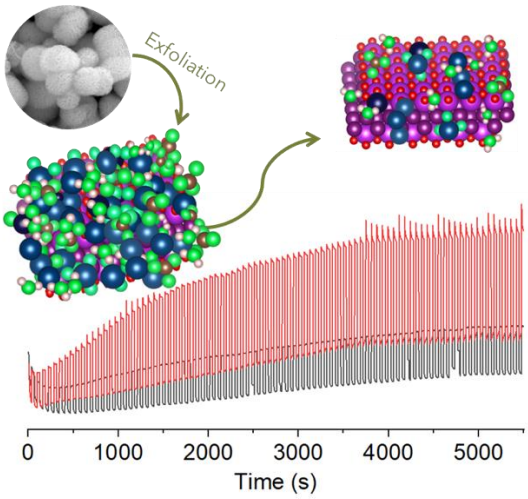


**TOC figure**

This work studies the surface chemistry of BiOI during photoelectrocatalytic water oxidation. BiOI nanosheets synthesized by microwave reaction and liquid phase exfoliation contain species like $CO_3^{2-}$, $Bi^{5+}$, $I_3^-$, $IO_3^-$ and hydroxides, which are tuned during long-term operation and create more active sites, thus enhancing the photocurrent and improving interfacial charge transfer.

Supporting Information

**Tuning surface chemistry in 2D layered BiOI by facile liquid-phase exfoliation for enhanced photoelectrocatalytic oxygen evolution**

*Mengjiao Wang, Jaime Gallego, Micaela Pozzati, and Teresa Gatti*

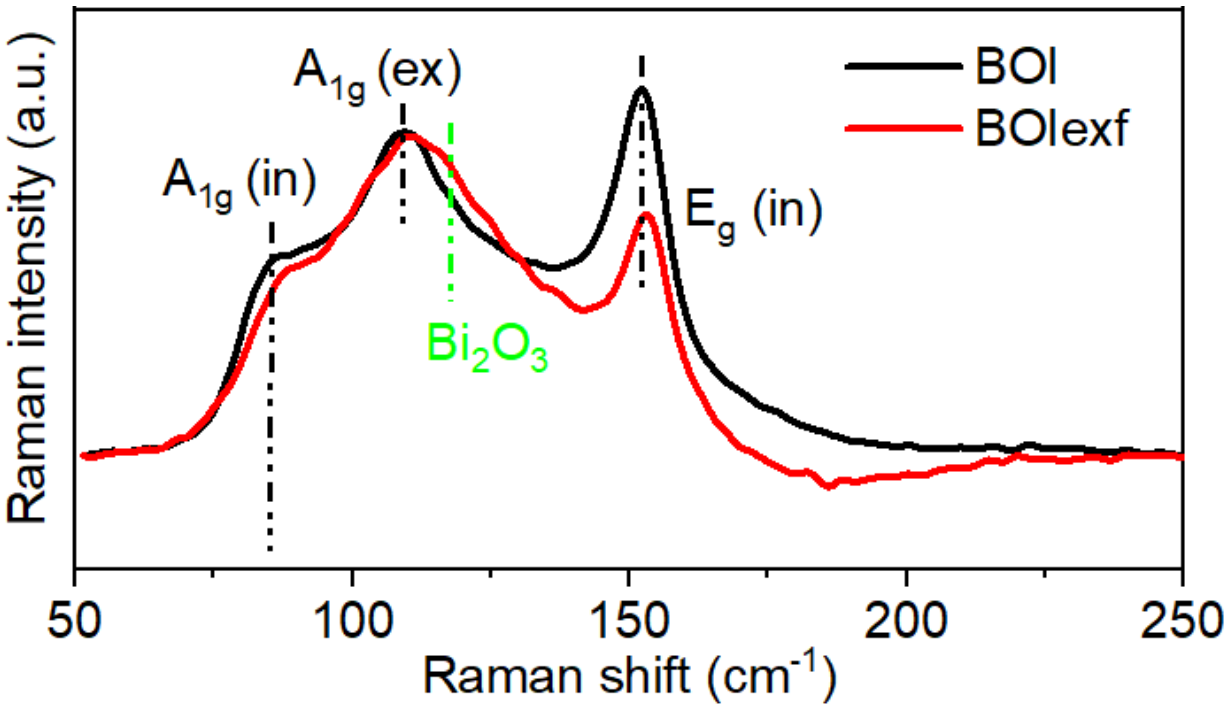


**Figure S1.** A close comparison of Raman spectra of BOI and BOIexf.

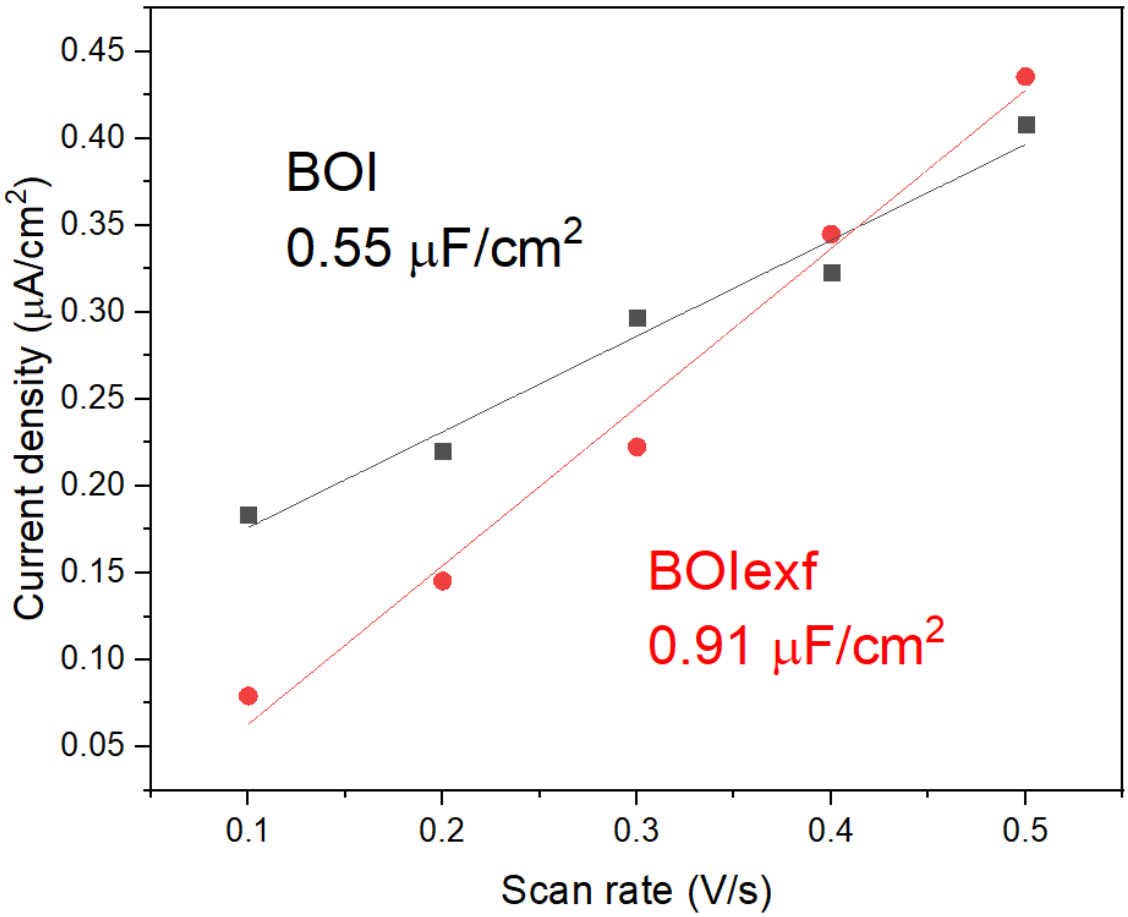


**Figure S2.** Estimated ECSA of BOI and BOIexf before OER.

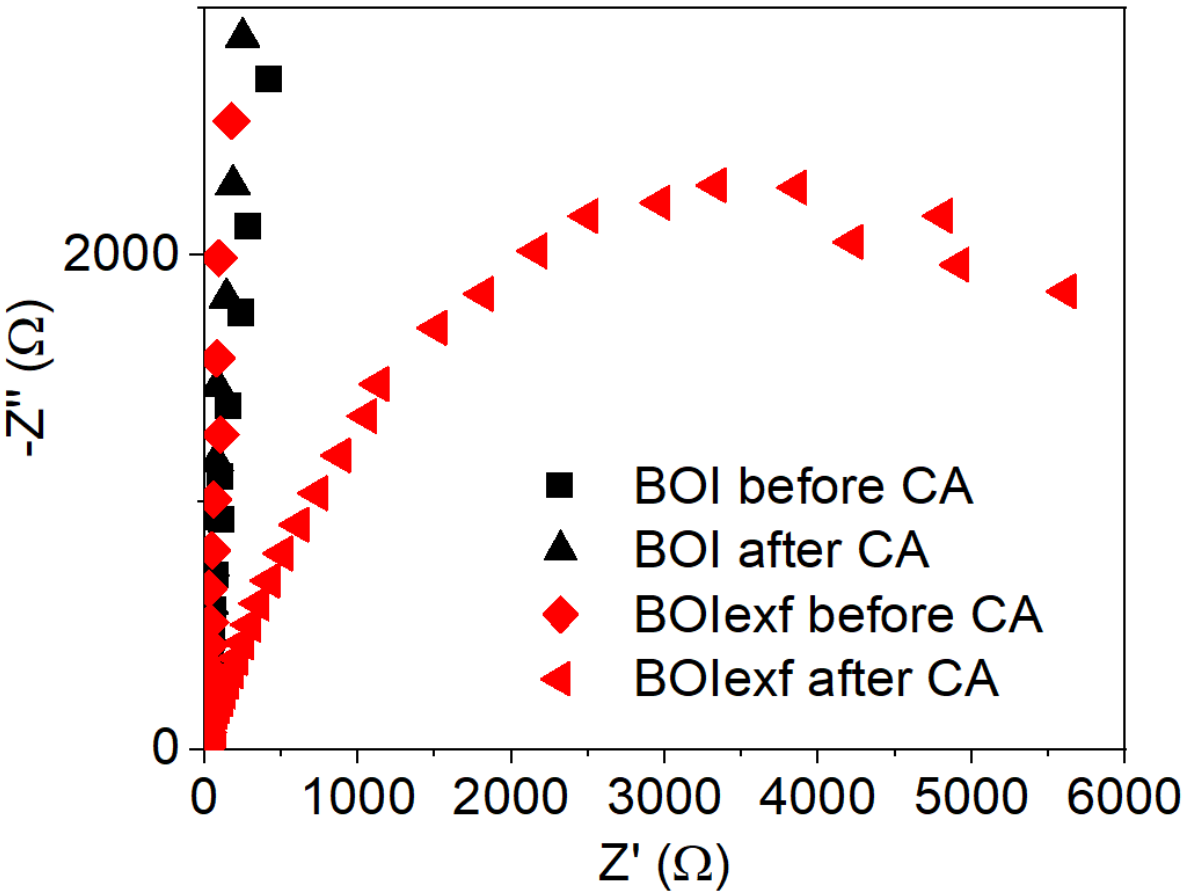


**Figure S3.** EIS of BOI and BOI exf before and after CA test.

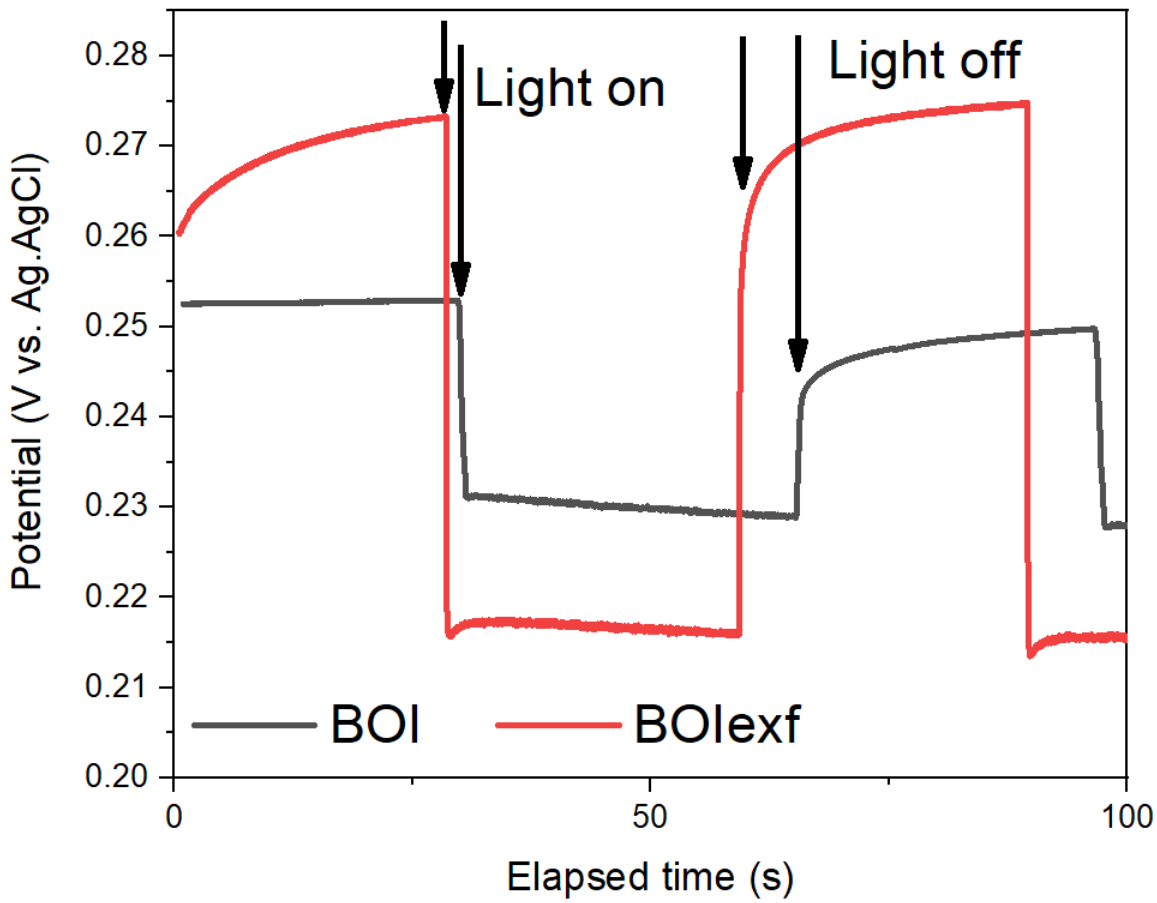


**Figure S4.** OCP decay profiles of BOI and BOIexf before the long-term CA test. The photovoltage of BOI and BOIexf is 22 mV and 59 mV, respectively.

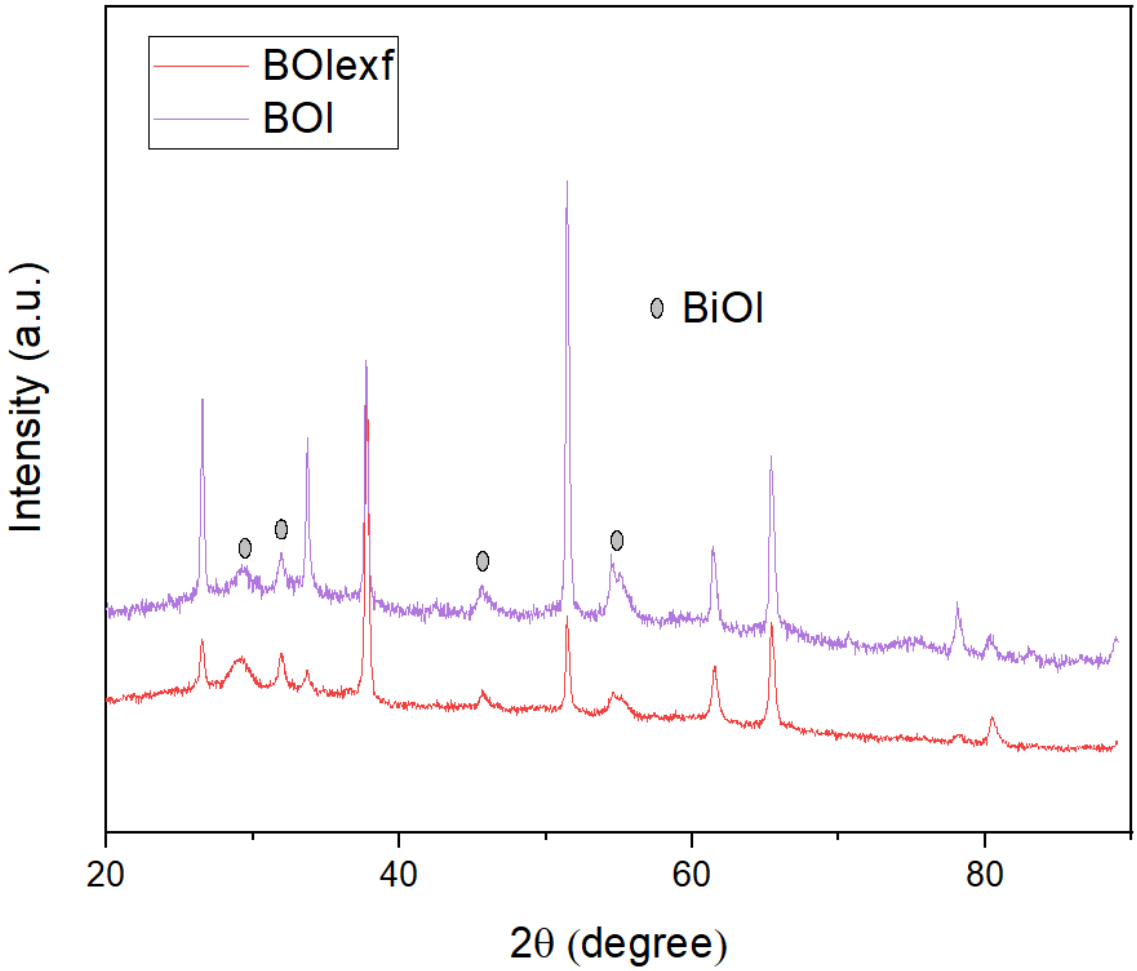


**Figure S5.** XRD patterns of BOI and BOIexf after PEC performance. All the other unlabeled peaks belong to FTO substrates.

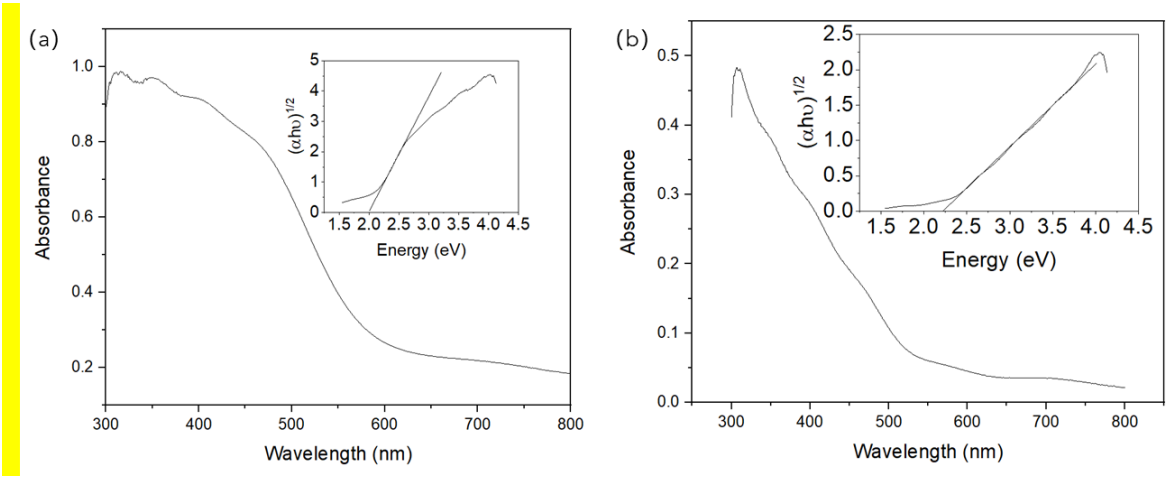


**Figure S6**. UV-vis spectra and Tauc Plot of (a) BOI and (b) BOIexf after CA.

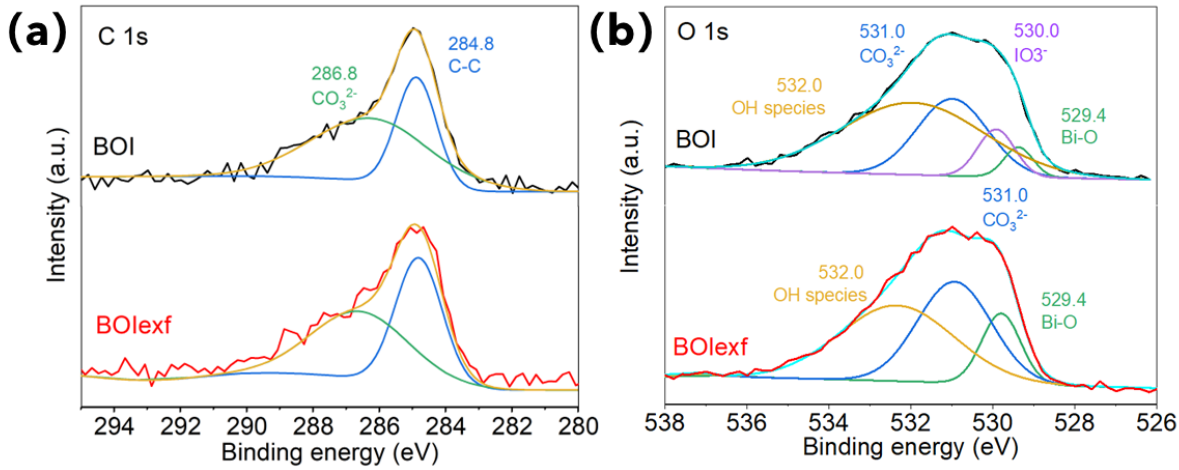


**Figure S7.** High-resolution XPS spectra of a) Bi 4f and b) I 3d of BOI and BOIexf after PEC OER.

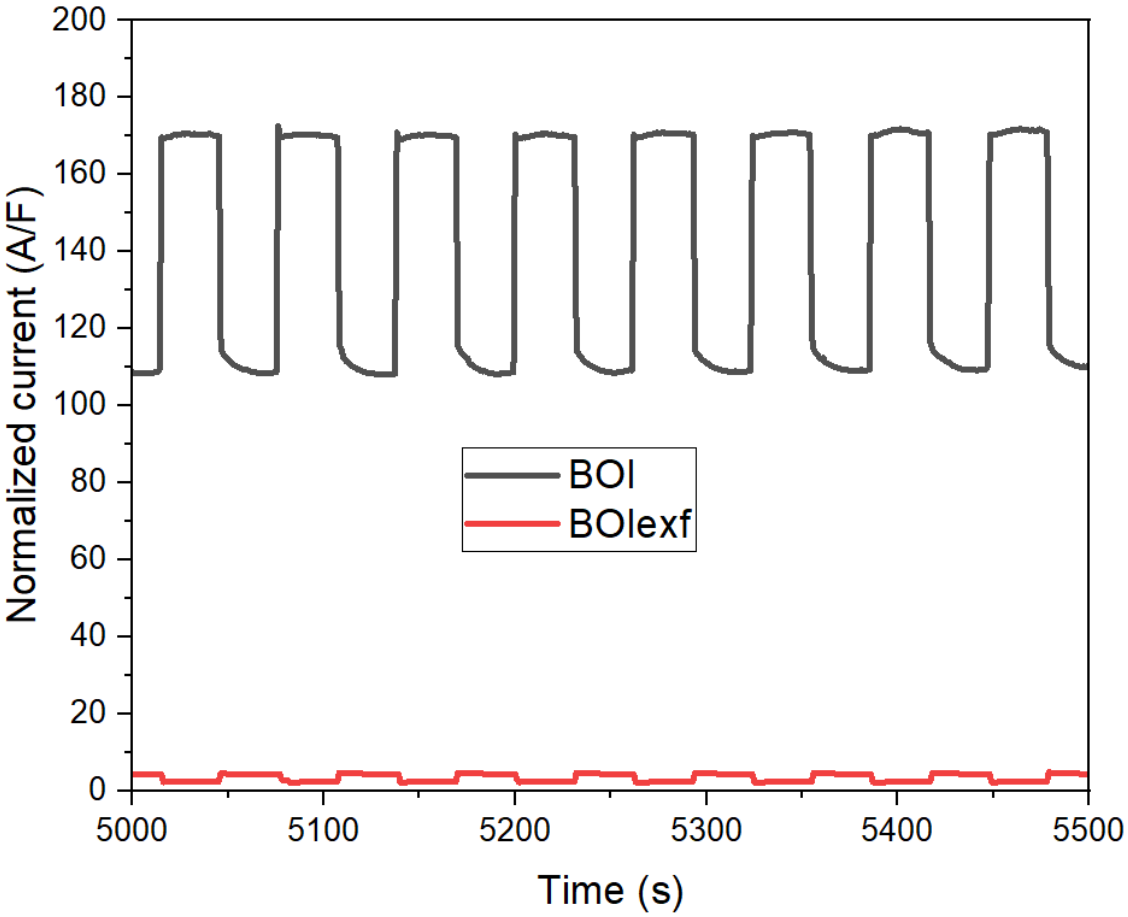


**Figure S8.** The ECSA-normalized photocurrent density of BOI and BOIexf after CA stabilization.

**Table S1.** fitting parameters of XPS spectra in Figure 2.

| sample | Peak name | Area fit | center | Max height | FWHM |
|---|---|---|---|---|---|
| BOI C 1s | $CO_3^{2-}$ | 2009.47505 | 287.84771 | 537.6747 | 3.511 |

| | | | | | |
|---|---|---|---|---|---|
| | C-C | 2573.99201 | 284.82436 | 1311.9946 | 1.84307 |
| BOIexf C1s | $CO_3^{2-}$ | 2153.69717 | 287.74983 | 419.18464 | 4.82666 |
| | C-C | 158.33768 | 284.82428 | 149.21885 | 0.99685 |
| BOI Bi $4f_{5/2}$ | $Bi^{5+}$ | 8354.8253 | 167.54169 | 4456.4707 | 1.76122 |
| | $Bi_2O_2$ | 9613.72915 | 164.8684 | 4156.67353 | 2.17277 |
| | $Bi_2O_3$ | 9216.00015 | 164.0175 | 7015.79703 | 1.23405 |
| BOI Bi $4f_{7/2}$ | $Bi^{5+}$ | 10356.6466 | 162.22808 | 5524.25018 | 1.76122 |
| | $Bi_2O_2$ | 12833.65683 | 159.52213 | 5548.87728 | 2.17277 |
| | $Bi_2O_3$ | 11418.84153 | 158.7116 | 8912.85002 | 1.25164 |
| BOIexf Bi $4f_{5/2}$ | $Bi^{5+}$ | 11405.5943 | 168.49066 | 7392.56672 | 1.44941 |
| | $Bi_2O_2$ | 21836.03008 | 166.69251 | 5987.0592 | 3.42632 |
| | $Bi_2O_3$ | 8825.87362 | 164.66753 | 4929.0222 | 1.68215 |
| BOIexf Bi $4f_{7/2}$ | $Bi^{5+}$ | 17114.01073 | 163.21534 | 11092.47188 | 1.44941 |
| | $Bi_2O_2$ | 28008.68792 | 161.09491 | 7679.63339 | 3.42632 |
| | $Bi_2O_3$ | 9922.07117 | 159.14223 | 5541.23433 | 1.68215 |
| BOI I $3d_{3/2}$ | $IO_3^-$ | 8591.37562 | 633.5007 | 4924.46996 | 1.63897 |
| | $I_3^-$ | 9802.23653 | 631.51599 | 6288.21697 | 1.46442 |
| | BiOI | 18056.12053 | 630.29831 | 14083.03464 | 1.20447 |
| BOI I $3d_{5/2}$ | $IO_3^-$ | 12313.59329 | 622.00412 | 7057.99636 | 1.63897 |
| | $I_3^-$ | 13513.11271 | 620.0119 | 8668.77114 | 1.46442 |
| | BiOI | 25506.80205 | 618.81853 | 19894.26104 | 1.20447 |
| BOIexf I $3d_{3/2}$ | $IO_3^-$ | 9314.03289 | 634.48465 | 6019.33746 | 1.45364 |
| | $I_3^-$ | 33666.58834 | 632.51188 | 6405.45199 | 4.93761 |
| | BiOI | 7578.00315 | 630.68436 | 3239.82354 | 2.19736 |
| BOIexf I $3d_{5/2}$ | $IO_3^-$ | 13047.76809 | 622.95998 | 8432.32997 | 1.45364 |
| | $I_3^-$ | 42335.84915 | 621.35876 | 8054.88382 | 4.93761 |
| | BiOI | 12794.95362 | 619.34219 | 5470.2294 | 2.19736 |
| BOI O 1s | $H_2O$ (ad) | 179.57082 | 533.77816 | 125.18404 | 1.34758 |
| | Hydroxide species | 1401.83464 | 532.53666 | 711.16241 | 1.85181 |
| | $CO_3^{2-}$ | 2739.05592 | 531.31621 | 844.38912 | 3.04738 |
| | $IO_3^-$ | 1352.92236 | 530.41404 | 1028.44089 | 1.23584 |
| | Bi-O | 3367.24526 | 529.18955 | 2579.24374 | 1.22645 |

| | | | | | |
|---|---|---|---|---|---|
| BOIexf O 1s | Physically adsorbed $H_2O$ | 991.16026 | 535.03642 | 455.07317 | 2.04612 |
| | $H_2O$ (ad) | 2993.427 | 533.4945 | 1709.69951 | 1.64481 |
| | $CO_3^{2-}$ | 3404.90596 | 531.3929 | 1340.52302 | 2.38615 |
| | $IO_3$- | 1040.40405 | 529.85871 | 750.72405 | 1.30194 |
| | Bi-O | 425.38107 | 528.82183 | 440.89086 | 0.90639 |

**Table S2.** Fitting parameters of XPS spectra in Figure 4.

| sample | Peak name | Area fit | center | Max height | FWHM |
|---|---|---|---|---|---|
| BOI Bi $4f_{5/2}$ | $Bi^{5+}$ | 13681.96974 | 166.34868 | 6157.23558 | 2.08752 |
| | $Bi_2O_2$ | 32363.33703 | 164.43126 | 19117.01937 | 1.59038 |
| BOI Bi $4f_{7/2}$ | $Bi^{5+}$ | 16122.65809 | 161.26913 | 7255.62108 | 2.08752 |
| | $Bi_2O_2$ | 40102.30636 | 159.11522 | 23688.45812 | 1.59038 |
| BOIexf Bi $4f_{5/2}$ | Bi5+ | 14799.73445 | 165.90469 | 4853.34396 | 4.50201 |
| | $Bi_2O_2$ | 34844.81386 | 164.43035 | 28695.54625 | 1.47237 |
| BOIexf Bi $4f_{7/2}$ | Bi5+ | 32098.22983 | 160.58019 | 6697.96745 | 4.50201 |
| | $Bi_2O_2$ | 44974.10208 | 159.11537 | 22232.53469 | 1.47237 |
| BOI I $3d_{3/2}$ | $IO_3^-$ | 296.70973 | 635.61287 | 180.10427 | 1.54766 |
| | $I_3^-$ | 2084.63942 | 632.17107 | 1018.68325 | 1.92247 |
| | BiOI | 4237.9235 | 630.39411 | 2457.76718 | 1.61987 |
| BOI I $3d_{5/2}$ | $IO_3^-$ | 705.34009 | 623.9272 | 428.66713 | 1.54577 |
| | $I_3^-$ | 3360.13506 | 620.98068 | 1629.44456 | 1.93725 |
| | BiOI | 6418.48118 | 618.88608 | 3726.45805 | 1.61809 |
| BOIexf I $3d_{3/2}$ | $I_3^-$ | 6288.06709 | 631.13975 | 1869.57105 | 3.15968 |
| | BiOI | 12231.37686 | 630.29428 | 7515.06621 | 1.52901 |
| BOIexf I $3d_{5/2}$ | $I_3^-$ | 9122.69501 | 620.16702 | 2663.63071 | 3.21749 |
| | BiOI | 18014.33733 | 618.83727 | 11068.15576 | 1.52901 |